

Vortex Patches under Cnoidal Waves

Christopher W. Curtis
Henrik Kalisch

Abstract

1 Introduction

The modeling of free-surface waves is a well studied and central area in several areas within applied mathematics, fluid mechanics, and oceanography. Analytical concerns have motivated almost two-hundred years of work with a corresponding slew of techniques both formal and rigorous that have found use throughout applied mathematics; see [1] and the historical notes contained therein. The free-surface problem also appears as a fundamental problem in both old [2] and modern [3] classics on fluid mechanics. Perhaps the greatest role that the problem plays though is in formulating the foundation for spectral-wave modelling, which forms the core of much of modern data-driven oceanography [4].

A long standing issue however in the modeling of free-surface waves is the impact that vorticity has on wave dynamics. This has been considered an especially difficult problem for general vorticity profiles given that the momentum equation cannot be readily integrated up to the surface via the use of a harmonic potential. Much progress has been made by making the simplifying assumption of the vorticity being a constant leading to seminal numerical and analytic studies of these problems; see [1, 5, 6, 7] among many others. In a similar vein, one can see the stability theory of shear profiles [8, 9, 10, 11] as another means of addressing the impact of vorticity on free surface flows. This approach has been pushed to higher-order-nonlinear models with corresponding numerical implementations in [12].

However, in neither case can one track the evolution of an arbitrary vortex profile. As shown in experiment [13, 14, 15], the motion of solitary waves over bathymetric features induces the formation of vortex patches. Likewise, it is clear that accurate near shore modeling involves an understanding of the fluid vorticity profile and its interactions with the free surface. Progress in this direction has been made by assuming shallow-water scalings and deriving various Boussinesq-like models [16, 17, 18] or Green-Naghdi models [19, 20, 21]. These approaches, while limited to near-shore conditions, allow markedly enhanced modeling of shoaling and can be coupled to phenomenological models of wave-breaking induced turbulence to allow for very accurate near-shore computation.

In contrast to the above work, a body of numerical methods has developed within computational fluid mechanics known as Point-Vortex Methods (PVMs). These are numerical schemes which track the evolution of compactly supported vorticity profiles via direct discretizations of the vorticity profile; see [22, 23, 24, 25, 26, 27] among several others. These schemes are especially attractive in that they do not place any strong restrictions on the flow and are suitable for simulations across a wide range of scales and geometries [28, 29]. It was then shown in [30] that, by incorporating the

methodology for reformulating the free-surface problem as found in [31], that PVMs could be in effect merged with Dirichlet-to-Neumann Operator (DNO) based methods [32, 33] for solving the free-surface problem.

However, in [30], simulations with at most four vortices were studied, preventing the modeling of more complicated vortex patches underneath free surface waves. Thus, in this paper we present simulations of vortex patches involving several thousands of vortices. To do so, we incorporate into the formulation in [30] many of the techniques for error control and computational efficiency that have been developed in the PVMs community. In particular the use of a Fast-Multipole Method [34] and Lagrangian-to-Eulerian regridding [23] play critical roles in obtaining our results. Using this machinery, by moving to shallow-water scalings, we are able to then study the impact of vortex patches on the evolution of free surface waves which are approximated by the cnoidal-solutions of the Korteweg–de Vries equation. This is a canonical model for nonlinear, shallow-water free surface waves, and it thus serves as an excellent source for the generation of families of initial conditions for the free-surface state. While requiring periodic boundary conditions, the approach in this paper allows for arbitrary depth and modeling accuracy, thus providing a distinct complement to the Boussinesq and Green-Naghdi models described above.

As we show, vortex patches can induce nontrivial deformations of a free surface wave. This deformation is more pronounced the more linear the surface wave is, or the better a small amplitude modal approximation is to the free surface. This can best be understood by examining the relative input of energy into the free surface. As shown, the less nonlinear the surface wave, the more energy it receives from the vortex patch, thereby creating high-frequency oscillations and thus significant distortions of the wave profile. Likewise, we see that the transport of the patch itself is significantly enhanced when larger amplitude, wider nonlinear-surface waves move over the patch, which pulls energy from the surface to increase its speed of propagation. An especially curious feature worth future study is that the mean energy transfer from wave to patch is more linear with increasing patch strength for more nonlinear waves. Why this is the case is not clear, and thus it motivates further future work.

An overview of the paper is as follows. In Section 2, the model, numerical scheme, and implementation details are presented. Section 3 presents our numerical results, while in Section 4 we summarize our results and speak to future directions. An Appendix collects technical details about the DNO.

2 Model, Numerical Scheme, and Implementation Details

Throughout, we are attempting to describe the simultaneous evolution of a free surface $y = \eta(x, t) + H$, and a compactly supported patch of vorticity $\omega(x, y, t)$ underneath the free surface. We suppose along the curve $z = 0$ that we have a solid boundary so that the normal velocity is identically zero. In an inviscid, incompressible fluid, we can represent the fluid velocity $\mathbf{u}(x, y, t)$ generated by a vortex patch characterized by vorticity profile $\omega(\mathbf{x}, t)$, $\mathbf{x} = (x, y)$, over the compact domain $\Omega(t)$ via the integral equation

$$\mathbf{u}(\mathbf{x}, t) = \int_{\Omega(t)} \mathbf{K}(\mathbf{x} - \tilde{\mathbf{x}}) \omega(\tilde{\mathbf{x}}, t) d\tilde{\mathbf{x}} + \nabla \tilde{\phi}, \quad \Delta \tilde{\phi} = 0.$$

where ω is the vorticity, and \mathbf{K} is the standard Biot-Savart kernel. The harmonic function $\tilde{\phi}$ is used to address boundary conditions as explained in [35]. An attractive means for discretizing this equation as summarized in [22] is to approximate the vorticity ω via the expression ω_d which is given by a collection of N point-vortices at positions $\mathbf{x}_j(t)$ via the PVM expansion

$$\omega_d(\tilde{\mathbf{x}}, t) = \sum_{j=1}^N \frac{\Gamma_j}{\delta^2} \chi\left(\frac{\tilde{\mathbf{x}} - \mathbf{x}_j(t)}{\delta}\right), \quad \mathbf{x}_j(t) = (x_j(t), y_j(t)), \quad (1)$$

where χ is some appropriately chosen mollifier, see [26], and Γ_j is the circulation associated with the point vortex at $\mathbf{x}_j(t)$. Thus, we can reduce the problem of tracking the evolution of the vortex patch to describing the motion of the point vortices via the system of ODE's

$$\frac{d\mathbf{x}_j}{dt} = \sum_{l \neq j}^N \Gamma_l \mathbf{K}_\delta(\mathbf{x}_j - \mathbf{x}_l) + \nabla \tilde{\phi}(\mathbf{x}_j, t), \quad \mathbf{K}_\delta(\mathbf{x}) = \frac{1}{\delta^2} \int_{\mathbb{R}^2} \mathbf{K}(\mathbf{x} - \tilde{\mathbf{x}}) \chi\left(\frac{\tilde{\mathbf{x}}}{\delta}\right) d\tilde{\mathbf{x}}.$$

Choosing, as in [26], the mollifier χ to be the fourth-order kernel

$$\chi(r) = 2e^{-r^2} - \frac{1}{2}e^{-r^2/2},$$

introducing periodic boundary conditions in the lateral direction and enforcing the presence of a solid boundary along the curve $y = 0$ then modifies the above dynamical system to be

$$i \frac{dz_j^*}{dt} = \frac{1}{2\pi} \left(\sum_{l \neq j}^N \Gamma_l \sum_{m=-\infty}^{\infty} \frac{\tilde{\chi}(z_j - z_l - 2Lm; \delta)}{z_j - z_l - 2Lm} - \sum_{l=1}^N \Gamma_l \sum_{m=-\infty}^{\infty} \frac{\tilde{\chi}(z_j - z_l^* - 2Lm; \delta)}{z_j - z_l^* - 2Lm} \right) + \partial_y \tilde{\phi} + i \partial_x \tilde{\phi},$$

where $z_j = x_j + iy_j$, the period in x is given by $2L$, and

$$\tilde{\chi}(r; \delta) = \left(1 - e^{-r^2/2\delta^2}\right) \left(1 + 2e^{-r^2/2\delta^2}\right).$$

We evaluate the corresponding sums over the image points $z_j - z_l^*$ so as to keep the zero flow through $y = 0$ condition strictly enforced.

Following the arguments in [30], and again emphasizing the compact support of the vorticity $\omega(x, y, t)$, we then have at the free surface the coupled nonlinear system

$$\partial_t \eta = -\partial_x \eta \partial_x \tilde{\phi} + \partial_y \tilde{\phi} + P_v,$$

and

$$\partial_t \tilde{\phi} + \frac{1}{2} \left| \nabla \tilde{\phi} \right|^2 + \text{Im} \{Q_v\} \partial_x \tilde{\phi} + \text{Re} \{Q_v\} \partial_y \tilde{\phi} + g\eta = E_v - \frac{1}{2} |Q_v|^2 \quad (2)$$

where we have defined

$$c(\eta, z_j) = \cot \left(\frac{\pi}{2L} (\eta + H - z_j) \right),$$

so that

$$P_v = \text{Re} \{Q_v\} - \text{Im} \{Q_v\} \partial_x \eta,$$

$$Q_v = \frac{1}{4L} \sum_{j=1}^N \Gamma_j (c(\eta, z_j) - c(\eta, z_j^*)),$$

and

$$E_v = \frac{1}{4L} \sum_{j=1}^N \Gamma_j (\dot{x}_j \text{Im} \{c(\eta, z_j) - c(\eta, z_j^*)\} + \dot{y}_j \text{Re} \{c(\eta, z_j) + c(\eta, z_j^*)\})$$

We present a brief derivation of Equation (2) in the Appendix for the sake of completeness. Note, we have ignored the mollification given the separation between the surface and the point vortices used to approximate the vortex patch.

Defining $q = \tilde{\phi}|_{z=\eta+H}$, standard arguments [32, 30] allow for the derivation of series representations to the Dirichlet-to-Neumann operator $G(\eta)$ so that

$$\eta_t = Gq + P_v,$$

and

$$\begin{aligned} \partial_t q + \frac{1}{2} (\partial_x q)^2 + g\eta - E_v + \frac{1}{2} |Q_v|^2 = \\ - \frac{1}{1 + (\partial_x \eta)^2} \left(\left(P_v + \text{Re} \{Q_v\} - \frac{1}{2} (Gq + \partial_x \eta \partial_x q) \right) (Gq + \partial_x \eta \partial_x q) + \text{Im} \{Q_v\} (\partial_x q - \partial_x \eta Gq) \right) \end{aligned}$$

Note, in the numerics, it is more convenient and in some ways more physically relevant to solve for the variable $Q = q_x$. We note that the DNO can readily be factored so that $G(\eta)q = \tilde{G}(\eta)Q$, and throughout the remainder of the paper, it is this version of the DNO we work with, though we drop the tilde for the sake of brevity. See the Appendix for a more complete description of details about the DNO.

Thus, the surface boundary conditions can be recast entirely in terms of surface variables alone. This then leaves the problem of evaluating the derivatives of $\tilde{\phi}$ at the vortex positions thereby allowing us to compute the speeds of the point vortices and closing the system of equations in terms of η , q , and z_j . To do this, we repeat the arguments in [30], where it was shown that

$$\partial_y \tilde{\phi} + i \partial_x \tilde{\phi} \Big|_{z_j} = -\frac{1}{4L} \int_{-L}^L ((c(\eta, z_j) - c^*(\eta, z_j^*)) \partial_x q - i(c(\eta, z_j) + c^*(\eta, z_j^*)) G(\eta)q) dx$$

Implementation Details for the Fast-Multipole Method

As can be seen, the presence of the mollifier prevents the closed form evaluation of the sums in m , thereby potentially adding significant overhead in numerical computations, even if fast Fourier transforms are used to evaluate the sums. We note however that

$$\tilde{\chi}(r; \delta) = 1 + \bar{\chi}(r), \quad \bar{\chi}(r) = \left(1 - 2e^{-r^2/2\delta^2}\right) e^{-r^2/2\delta^2}$$

which tacitly explains the role of mollification, which is to remove singularities in the determination of particle velocities when $|z_j - z_l| \lesssim \delta$. Thus, when we know that $|z_j - z_l| > \delta$, we take $\tilde{\chi}(r; \delta) \sim 1$ so that

$$\frac{1}{2\pi} \sum_{m=-\infty}^{\infty} \frac{\tilde{\chi}(z_j - z_l - 2Lm; \delta)}{z_j - z_l - 2Lm} \approx \frac{1}{4L} \cot \left(\frac{\pi}{2L} (z_j - z_l) \right),$$

where the sum is taken in the principal value sense. In the case that $|z_j - z_l| \lesssim \delta$, we use instead

$$\frac{1}{2\pi} \sum_{m=-\infty}^{\infty} \frac{\tilde{\chi}(z_j - z_l - 2Lm; \delta)}{z_j - z_l - 2Lm} \approx \frac{1}{4L} \cot\left(\frac{\pi}{2L}(z_j - z_l)\right) + \frac{1}{2\pi} \frac{\bar{\chi}(z_j - z_l; \delta)}{z_j - z_l}.$$

The error incurred in these approximations is only exponentially small.

However, even in the best case scenario, the evaluation of the particle velocities is an $\mathcal{O}(N^2)$ operation, and as we show later, we should anticipate there being large numbers of vortices in order to maintain the accuracy of our simulation. That being said, by employing a multi-level Barnes-Hut algorithm, which is an example of a Fast-Multipole Method (FMM) [34], we can reduce the evaluation of the sums used to compute particle velocities to an $\mathcal{O}(N \log N)$ operation. Further, our use of a FMM for the evaluation of the velocities \dot{z}_j in effect determines all points either far or close to z_j , and thus it naturally selects when to use approximations appropriate for the cases $|z_j - z_l| \leq \delta$ or $|z_j - z_l| > \delta$. The method relies crucially on the rapid convergence of the approximation

$$\cot(\tilde{z}_j - \tilde{z}_l) \approx \frac{(1 - \tan(\tilde{z}_j - c) \tan(c - \tilde{z}_l))}{\tan(\tilde{z}_j - c)} \sum_{m=0}^p (-1)^m \frac{\tan^l(c - \tilde{z}_l)}{\tan^l(\tilde{z}_j - c)},$$

where

$$\tilde{z} = \frac{\pi}{2L} z, \quad |\tilde{z}_l - c| < |\tilde{z}_j - c|.$$

Throughout the remainder of the simulations, we choose $p = 10$, which provides the necessary speed-up without sacrificing any significant accuracy in the computation of the point-vortex velocities.

Shallow-Water Scalings and the KdV equation

So that we can work in a shallow-water environment, we introduce the scalings

$$\tilde{x} = \frac{x}{\lambda}, \quad \tilde{y} = \frac{y}{H}, \quad \tilde{t} = \frac{\sqrt{gH}}{L} t, \quad \eta = d\tilde{\eta}, \quad \tilde{\phi} = \mu L \sqrt{gH} \tilde{\phi}, \quad \tilde{\Gamma}_j = \frac{\Gamma_j}{\Gamma},$$

where we define the non-dimensional parameters

$$\mu = \frac{d}{H}, \quad \gamma = \frac{H}{\lambda}.$$

Note, in this scaling, we see that the vorticity ω is then scaled as

$$\omega = \frac{\mu \sqrt{gH}}{H} \tilde{\omega},$$

so that by using Stoke's theorem, we see the net circulation Γ can be written as

$$\Gamma = \mu L \sqrt{gH} \tilde{\Gamma}, \quad \tilde{\Gamma} = \int_{\tilde{\Omega}} \tilde{\omega} d\tilde{A}.$$

Throughout the paper, we make reference to the nondimensional Froude number F to characterize the strength of the vortex patch. In these coordinates, it is given by

$$F = \frac{\Gamma}{\mu \lambda \sqrt{gH}}.$$

In the absence of vorticity, one can readily show that in the traveling coordinate $\xi = x - t$ that the long time evolution of the tangential surface velocity $Q = q_x$ and the surface η are found via the Korteweg–de Vries (KdV) equation,

$$2\partial_\tau Q + 3Q\partial_\xi Q + \frac{1}{3}\partial_\xi^3 Q = 0.$$

As is known, the KdV equation has an infinite number of periodic traveling wave solutions of the form

$$Q(x, t) \sim q_0 + 8\tilde{m}^2 \kappa^2 \text{cn}^2(\kappa(x - (1 + \mu\tilde{c})t); \tilde{m}), \quad (3)$$

where

$$\tilde{c} = \frac{2}{3}\kappa^2(2\tilde{m}^2 - 1) + \frac{3}{2}q_0,$$

and where $0 \leq \tilde{m} < 1$ is the elliptic modulus of the cnoidal function $\text{cn}(\cdot; \tilde{m})$ and where $\mathcal{K}(\tilde{m})$ represents the complete elliptic integral of the first kind. This then implies that the surface profile is to leading order given by $\eta \sim Q$. We then choose initial conditions in our numerical simulations of free surface waves over vortex patches consistent with the traveling wave solutions of the KdV equation. Throughout the remainder of the paper, $q_0 = 0$.

Implementation Details for the Lagrangian to Eulerian Regridding

As noted in [26] and examined in [22] and related papers, a major source of error in PVMs is the implicit grid distortion induced by the Lagrangian flow of the particles $\mathbf{x}_j(t)$. In particular, we can interpret the mollification parameter δ as setting an effective radius of influence for each point $\mathbf{x}_j(t)$. The convergence theory associated with the PVM approximation, see [36], requires that if the particles \mathbf{x}_j start on a uniform mesh with mesh spacing h , then $h < \delta$, and this ‘overlapping’ must be maintained for all times of the simulation.

An especially effective means to ensure this was introduced in [23], where at some fixed number of time steps, the set of potentially irregular point positions and circulations, say

$$\{\mathbf{x}_j(t), \Gamma_j\}_{j=1}^N$$

are mapped onto a new, regularly h -spaced set of positions and corresponding circulations, say

$$\{\tilde{\mathbf{x}}_l, \tilde{\Gamma}_l\}_{l=1}^{\tilde{N}}.$$

This is done through the choice of a compactly supported interpolation kernel $\Lambda(\cdot)$ so that

$$\tilde{\Gamma}_l = \sum_{j=1}^N \Gamma_j \Lambda\left(\frac{\tilde{x}_l - x_j}{h}\right) \Lambda\left(\frac{\tilde{y}_l - y_j}{h}\right).$$

As in [23], we choose the kernel $\Lambda(x)$ so that

$$\Lambda(u) = \begin{cases} 1 - u^2, & 0 \leq |u| < \frac{1}{2} \\ \frac{1}{2}(1 - u)(2 - u), & \frac{1}{2} \leq |u| \leq \frac{3}{2} \\ 0, & |u| > \frac{3}{2} \end{cases}$$

h	N_s	N_f
.005	1252	11221
.0067	698	8385
.01	308	5937

Table 1: For varying grid spacings, h , the starting particle count N_s and the ending particle count N_f . The increase is a consequence of the regridding procedure, which in this case is done every six time steps of the simulation.

This choice ensures that the net circulation and the associated first and second moments are preserved after regridding. It should be noted however that regridding in this way generically increases the total particle count so that $\tilde{N} > N$. This is largely due to having to add points $\tilde{\mathbf{x}}_l$ relative to the distorted points \mathbf{x}_j furthest from the interior of the support of $\omega(\mathbf{x}, t)$.

We now model the initial vorticity via the circularly symmetric, compactly supported vorticity profile

$$\omega_0(r) = \begin{cases} \omega_m \left(1 - \frac{r^2}{R_v^2}\right)^3, & r \leq R_v \\ 0, & r > R_v \end{cases}$$

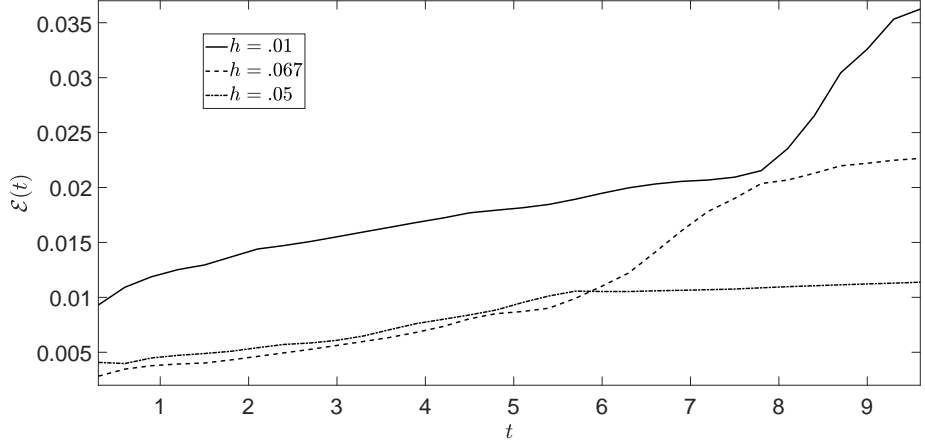
Given the circular symmetry of the profile, in the absence of a free surface or solid boundary, we know that $\omega(\mathbf{x}, t) = \omega_0(r)$. Using Equation (1) then, we can define a relative error $\mathcal{E}(t)$ via the formula

$$\mathcal{E}(t) = \left(\frac{\sum_{l=1}^{\tilde{N}} |\omega_d(\tilde{\mathbf{x}}_l, t) - \omega(\tilde{\mathbf{x}}_l, t)|^2}{\sum_{l=1}^{\tilde{N}} |\omega(\tilde{\mathbf{x}}_l, t)|^2} \right)^{1/2}.$$

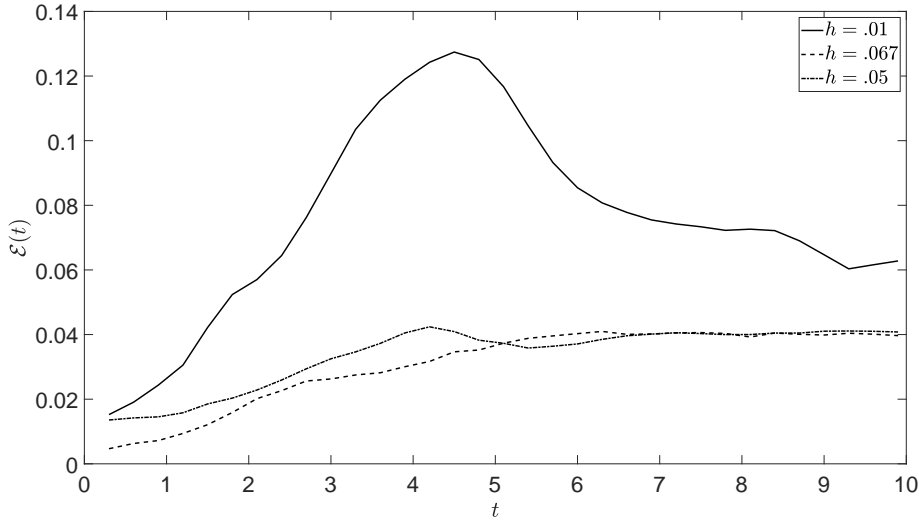
After introducing the shallow-water scalings described above, we choose $\mu = .2$, $\gamma = \sqrt{\mu}$, $\omega_m = 1$, and we run the simulations for $0 \leq t \leq t_f = 10 = 2/\mu$. Choosing a sampling rate of six time steps with $dt = .05$ and $\delta = 2h$, we produce the following error profiles for $h = .005$, $.0067$, and $.01$ in Figure 1. As can be seen, while the overall error percentages are quite small in all cases, as one would expect, choosing $h = .005$ and then maintaining that throughout the length of the simulation produces the most stable error profile.

However, the accuracy of the method must be contrasted against the computational expense incurred by introducing greater number of point-vortices at each regridding event. If we define N_s to be the initial number of point vortices and N_f to be the final number, we get the following table for differing values of h over the time interval $0 \leq t \leq t_f$. Likewise, for the range of vorticity strengths we wish to examine, we see by comparing Figures 1 (a) and (b) that choosing $h = .0067$ provides a relatively high-degree of accuracy while keeping the number of point vortices in the simulation at a more manageable level. We therefore stick with this particle spacing throughout the rest of the paper.

The increase in particle count and also position relative to the interior of the vorticity profile also raises the question of newly introduced points running into either the solid boundary at $z = 0$ or the free surface at $y = \epsilon\eta(x, t) + 1$. We therefore modify the interpolation scheme so that vortices do not propagate past either $z = 0$ or $z = .9$. Thus, while maintaining the accuracy of the PVM, this approach introduces significant overhead in the computation of particle velocities, which again is ameliorated through the use of a FMM.



(a) $\omega_m = 1$



(b) $\omega_m = 10$

Figure 1: Error profiles for $h = .005$, $.0067$, and $.01$ with $\delta = 2h$, $\omega_m = 1$ (a), $\omega_m = 10$ (b), and regridding done at every six time steps of the simulation.

3 Results

Throughout this section, we take $L = \lambda M$, where M counts the number of characteristic wavelengths included in the computational domain. Correspondingly, we take $M = \mathcal{K}(\tilde{m})/\kappa$, so that the period of the numerical simulation is equal to the period of the cnoidal wave. We note that this does place some limits on the overall elliptic modulus we may pick since as $\tilde{m} \rightarrow 1^-$, the solitary wave limit moves the periodic copies of the vortices in the lateral direction off to infinity. This creates a series of source terms in the free boundary equations which decay only quadratically, thereby radically limiting the efficacy of a spectral method for modeling the surface. This is a complication

beyond the scope of the present paper, but one that will be explored in future research.

With regards to the details of the simulations, we let $\mu = .2$, $\gamma = \sqrt{\mu}$, which is consistent with the KdV approximation, and $t_f = 2/\mu$, so that nonlinearity has enough time to have a significant impact. Twenty terms are taken in the recursive computation of the DNO, and a total of $K_T = 512$ modes are used for the pseudospectral approximation of the free surface. A Runge-Kutta 4 method with integrating factors is used with a time-step of $\delta t = .05$. We then have for our choice of vortex patch that F is given by

$$F = \frac{\pi\omega_m R_v^2}{4\gamma}.$$

The radius of the patch, R_v , is chosen so that

$$R_v = \frac{\gamma}{2} \min\{1 - y_c, y_c\}$$

where y_c is the initial vertical displacement of the patch. We choose $y_c = .35$, so that $R_v \approx .1565$. The initial horizontal displacement is $x_c = 0$. The initial position of the wave is at $x = -M/2$.

With these choices fixed, we note that the unscaled amplitude of the cnoidal wave initial conditions is given by $8(\tilde{m}\kappa)^2$. Throughout our simulations we have chosen κ for a given choice of elliptic modulus \tilde{m} so as to make this unscaled amplitude as close to unity as possible while still maintaining convergent numerical simulations. The issue for convergence in the DNO is a complicated one [33, 37], though the issue then can be mollified by reducing the size of μ . This of course adds further choices in parameters, which are already numerous as is. While in this paper we have chosen to stick the with DNO approach due to its relative ease of implementation, there are similar but more stable approaches such as the Transformed Field Expansion [38] which should be adaptable to this problem. Exploring this issue is a subject of future research.

In each of the following plots, we look at both the evolution of the vortex patch, and a comparison of the evolution of the free surface from the same initial conditions. Solid lines correspond to results in which $F \neq 0$ while dashed lines correspond to the zero vorticity, or $F = 0$, case. To better understand the impact of vortex patches on the cnoidal wave profiles examined in this work, we also provide a more quantitative measure of the impact of the vortex patch. This is done by plotting a relative comparison of the total energy in the surface, where the total energy in the surface in the shallow-water coordinates is given by

$$E(t; F) = \frac{1}{2} \int_{-M}^M (qG(\eta)Q + \eta^2) dx, \quad Q = q_x,$$

where we have emphasized the role of the patch through the implicit inclusion of the parameter F . In the absence of a vortex patch, i.e. $F = 0$, $E(t; 0)$ is a conserved quantity of the flow since it serves as the Hamiltonian of the dynamical system describing the surface dynamics [39]. Thus, in the following figures, we plot the relative difference in energy $\delta E(t; F)$ where

$$\delta E(t; F) = \frac{E(t; F) - E(t; 0)}{E(t; 0)}.$$

We likewise compute the mean relative-energy input δE_m where

$$\delta E_m = \frac{1}{t_f} \int_0^{t_f} \delta E(t; F) dt = \frac{1}{E(t; 0)} \left(\frac{1}{t_f} \int_0^{t_f} E(t; F) dt - E(t; 0) \right),$$

where in the last equality we have used the fact that $E(t; 0) = E(0; 0)$ since it is a conserved quantity of the flow. Finally, we also track the horizontal center-of mass of the vortex patch, say $x_c(t)$, defined by the formula

$$x_c(t) = \frac{\int_{\tilde{\Omega}(t)} x \tilde{\omega}(x, y, t) d\tilde{A}}{\int_{\tilde{\Omega}(t)} \tilde{\omega}(x, y, t) d\tilde{A}},$$

thereby allowing us to better understand the impact of the traveling wave on the motion of the patch.

Initially Quiescent Surface

To develop intuition and establish base line metrics with which to compare later results, we study an initially quiescent surface so that $\eta(x, 0) = 0$, and $\tilde{\phi}(x, 0)$ is chosen so as to make the initial surface velocity identically zero. We take the domain to be $-4 \leq x \leq 4$, which is comparable to the later domain sizes. Taking $F = .1$, representing the high end of the cases we examine later in the paper, we then generate Figure 2.

As seen, the patch induces significant deformations of the surface, though they are relatively small. Interestingly, the energy input rapidly saturates and then decreases while the patch slowly moves from left to right. That the displacement of the horizontal center-of mass of the patch only gets to about $x = .07$ for $t_f = 2/\mu = 10$ shows the impact of the solid boundary at $y = 0$ is relatively weak.

Elliptic Modulus $\tilde{m} = .3$

Taking $\tilde{m} = .3$ and $\kappa = .5$, this corresponds to $M \approx 3.3$. Taking $K_T = 512$, this gives $\delta x = .013$. The unscaled amplitude of the cnoidal initial conditions is given by $8(\tilde{m}\kappa)^2 \approx .18$. From both the pointwise comparisons in Figure 3 and the relative energy inputs in Figure 3, we see that stronger vorticity corresponds to greater deformation of the surface wave relative to the undisturbed case, and comparing across Figures 5 and 7, we see that the vortex patch has the strongest impact on the least nonlinear waves.

Moreover, we see in Figure 3 that the response of the relative energy input $\delta E(t; F)$ is nonlinear in F , with positive peaks being significantly enhanced over negative troughs. This nonlinear response is also seen in the values of the mean relative-energy inputs, δE_m , listed in Table 2. Moreover, the values of δE_m are always negative, implying energy is on average taken from the wave, which in part explains the decrease in the amplitude of the waves seen in Figures 3 (a), (c), and (e). The increased mean energy transfer seen in Table 2 also explains the strong deformations seen in comparing Figures 3 (b), (d), and (f) and shows how for a relatively linear surface profile, the vortex patch becomes a source of nonlinear interaction and wave mixing.

Examining Figure 4, we see that the center of mass of the patch has been displaced on average about .25 non-dimensional units relative to its starting position, which is significantly further than in the quiescent surface case examined above. The periods of acceleration seen by examining the center-of-mass positions in Figures 4 (b), (d), and (f) correspond to the wave crest moving over the patch. The difference in final displacement of the patch increases with increasing Froude number, which is to be expected due to the influence of the solid boundary; see the left-hand side of Figure

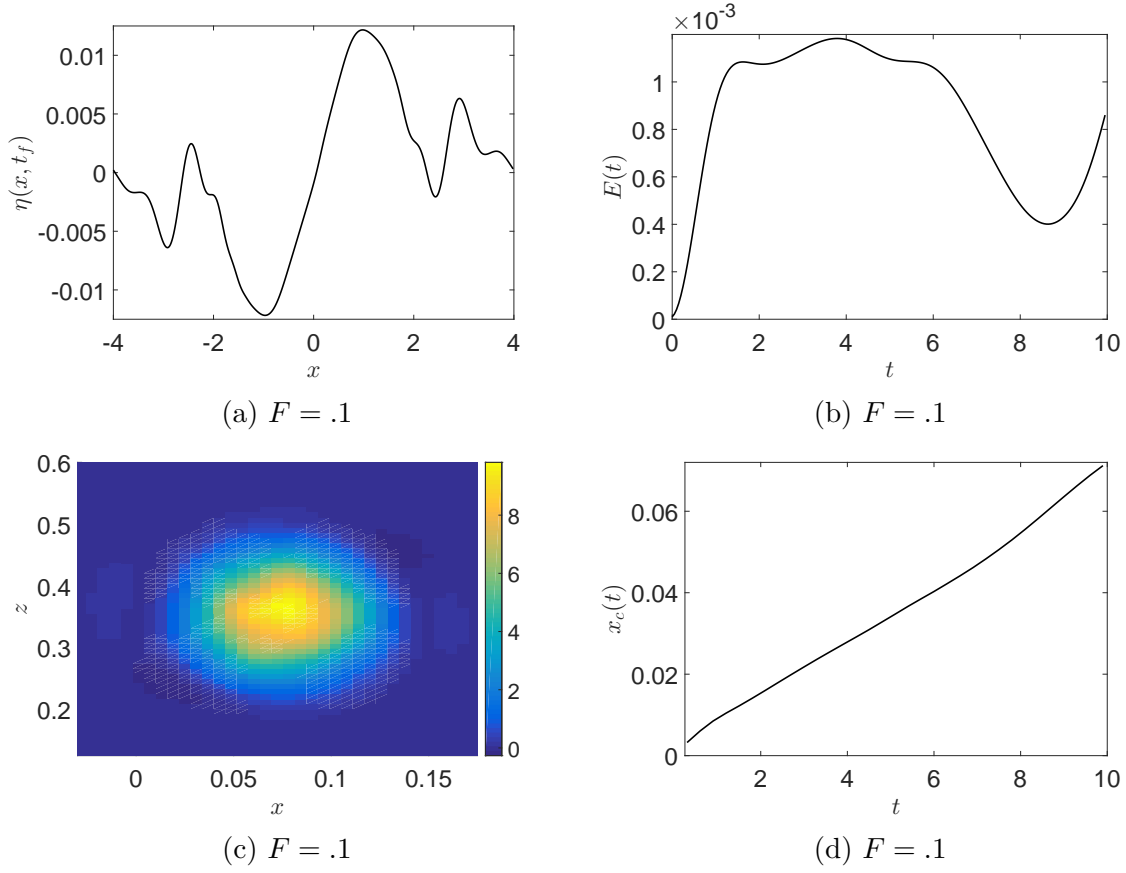
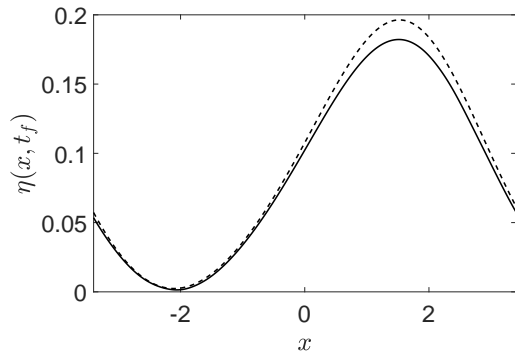


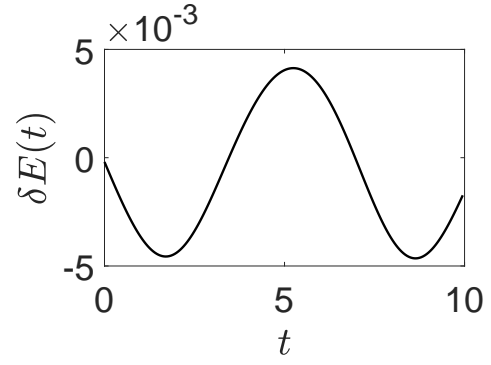
Figure 2: Profile (a), energy input (b), final vortex patch position and shape (c), and motion of the patch's horizontal center-of mass (d) for an initially still surface. Here $F = .1$, $\mu = .2$, $\gamma = \sqrt{\mu}$, and $t_f = 2/\mu$.

F	δE_m
.01	-1×10^{-3}
.05	-3.6×10^{-3}
.1	-3.7×10^{-3}

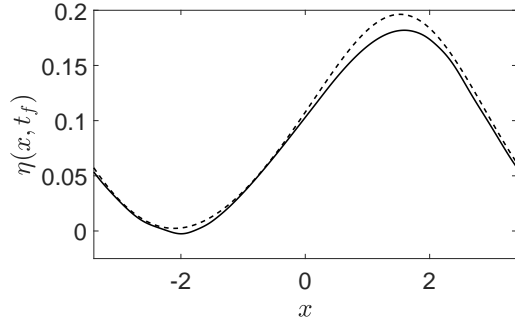
Table 2: Mean relative-energy input for $\tilde{m} = .3$ and $\kappa = .5$.



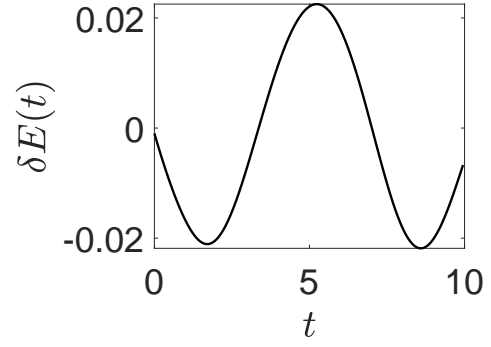
(a) $F = .01$



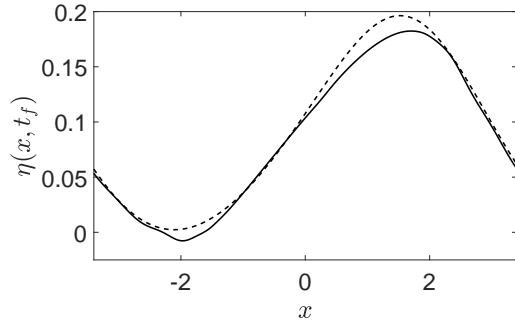
(b) $F = .01$



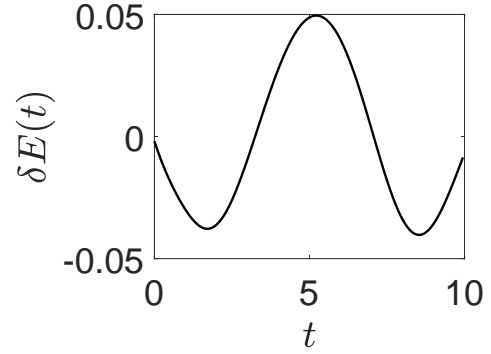
(c) $F = .05$



(d) $F = .05$



(e) $F = .1$



(f) $F = .1$

Figure 3: Comparisons of a cnoidal wave over a vortex patch(-) to a cnoidal wave over an irrotational fluid (- -) are shown on the left for various values of the Froude number F , while the relative energy change $\delta E(t)$ is shown on the right. Here $\mu = .2$, $\gamma = \sqrt{\mu}$, $t_f = 2/\mu$, $\tilde{m} = .3$, $\kappa = .5$.

F	δE_m
.01	-1.7×10^{-4}
.05	-7×10^{-4}
.1	-1.1×10^{-3}

Table 3: Mean relative-energy input for $\tilde{m} = .6$ and $\kappa = .43$.

4. However, it is clear that the solid boundary as a means of patch transport has minimal influence.

Elliptic Modulus $\tilde{m} = .6$

Taking $\tilde{m} = .6$, we find that $\kappa = .43$, this corresponds to $M \approx 4.4$. Taking $K_T = 512$, this gives $\delta x = .0172$. The unscaled amplitude of the cnoidal initial conditions is given by $8(\tilde{m}\kappa)^2 \approx .53$. As seen in Figure 5, we see that the larger elliptic modulus and larger amplitude makes the surface wave less responsive to the impact of vorticity. Nevertheless, the patch consistently lowers maximum amplitudes, and when large enough, induces significant oscillations in the surface profile.

However, in contrast to the $\tilde{m} = .3$ case above, we see that the response of the relative energy input $\delta E(t; F)$ is far more linear in nature, with peaks and troughs being enhanced about equally with rising values of F . The mean relative-energy inputs δE_m listed in Table 3 bear this more linear response out, though again the values are always negative implying again that energy is lost from the wave and put into the patch.

In Figure 6, we see that a relatively larger amplitude, wider surface wave is able to displace the patch significantly further, with mean displacement about .525 non-dimensional units. Again, while the impact of the solid wall along the bottom allows for greater displacement due to larger Froude number, this is nowhere near as significant as the impact of the wave on the patch.

Elliptic Modulus $\tilde{m} = .9$

Taking $\tilde{m} = .9$, we find that $\kappa = .35$, this corresponds to $M \approx 7.4$. Taking $K_T = 512$, this gives $\delta x = .029$. The unscaled amplitude of the cnoidal initial conditions is given by $8(\tilde{m}\kappa)^2 \approx .8$. Thus, somewhat surprisingly, we could use the largest amplitude wave when the initial condition was closest to that of a solitary wave profile. Likewise, aside from causing a slight broadening and thus decrease in maximum amplitude of the near solitary wave, vorticity has the least relative impact on the wave. Thus, if we treat the $\tilde{m} = .9$ as the ‘most’ nonlinear of the three cases examined, since this corresponds to the case closest to that of a nonlinear solitary wave, we see vorticity has the least overall impact on the most nonlinear of waves. This is especially seen by the weak response of $\delta E(t; F)$ plotted in Figure 7. We also get the clearest correlation between the loss in amplitude seen in Figure 7 and the relative energy input, which is largely negative though stretched out over a longer time scale than in comparison to the energy dynamics seen above. Looking at the relative energy-input means in Table 4, we see the most linear response to increasing Froude number compared to the more linear waves examined above.

We also see in Figure 8 that the center of the patch is displaced at the greatest distance relative to its starting position, showing the strong effect that relatively large amplitude, wide nonlinear waves have on the patch. Note, across the values of \tilde{m} and κ used throughout this section, the KdV

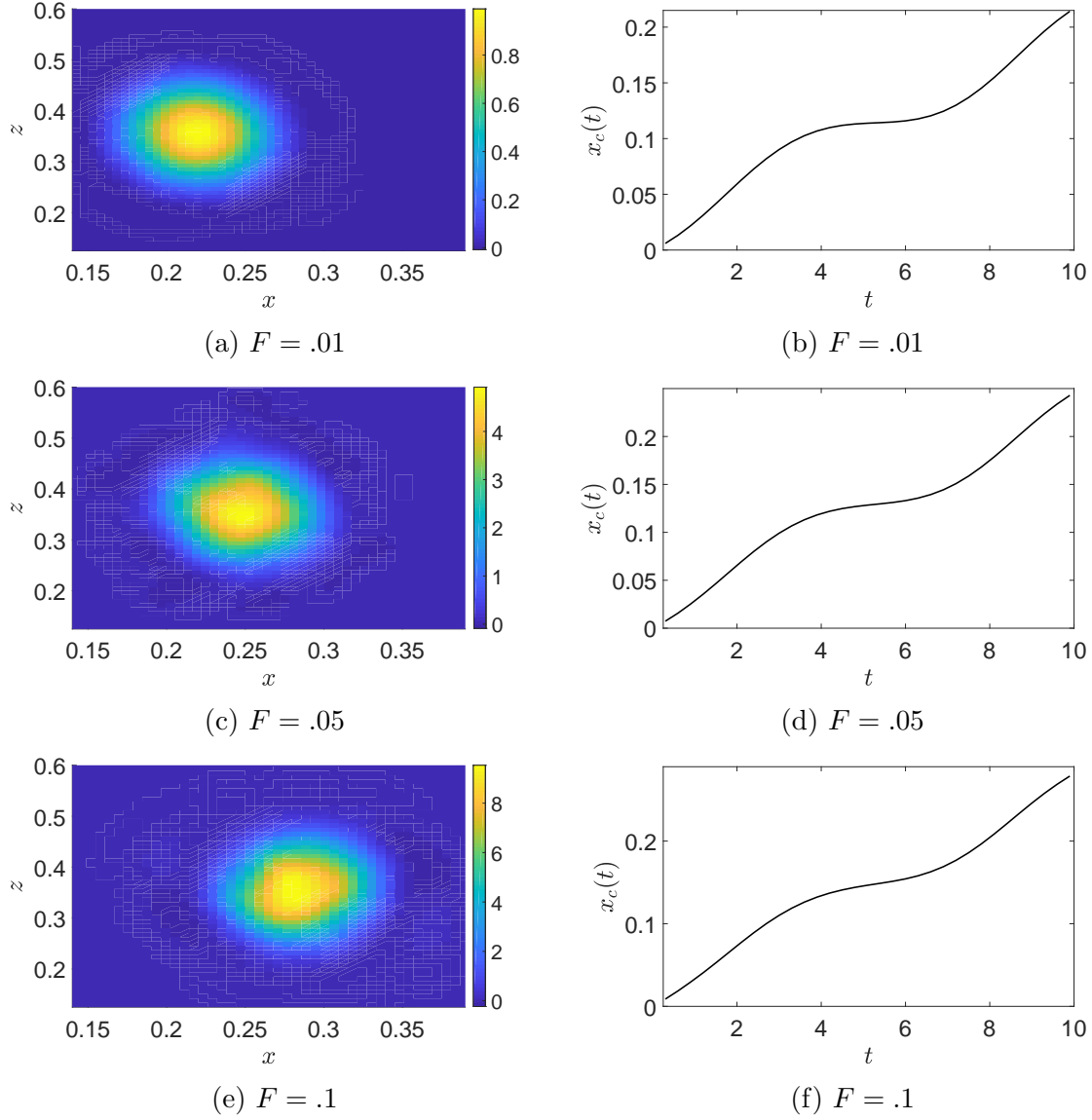


Figure 4: The vortex patches at the final time t_f for $F = .01$ (a), $F = .05$ (c), and $F = .1$ (e) and the motion of the horizontal center of mass $x_c(t)$ for $F = .01$ (b), $F = .05$ (d), and $F = .1$ (f) for $\tilde{m} = .3$ and $\kappa = .5$.

F	δE_m
.01	-3.87×10^{-4}
.05	-1.9×10^{-3}
.1	-3.7×10^{-3}

Table 4: Mean relative-energy input for $\tilde{m} = .9$ and $\kappa = .35$.

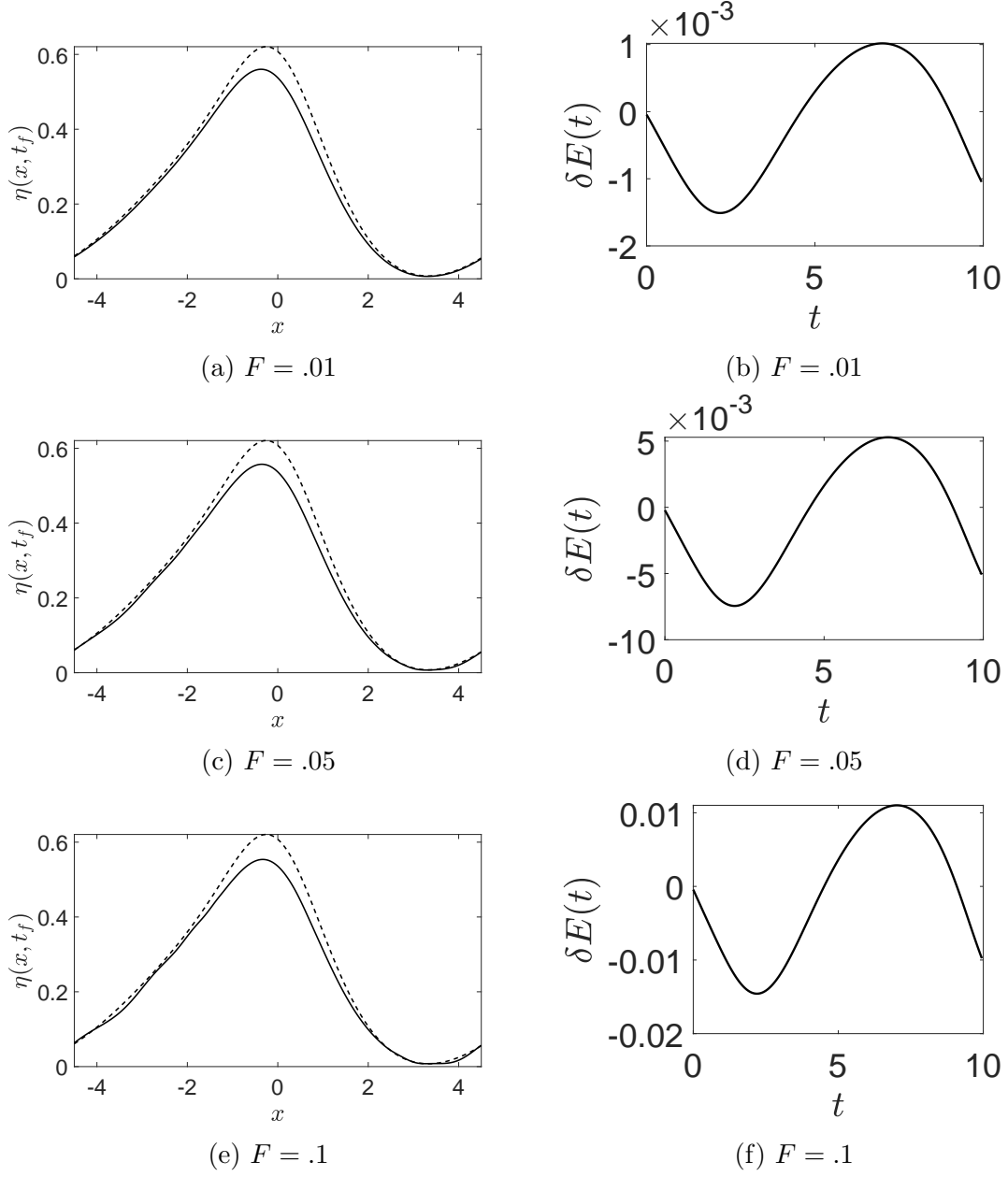
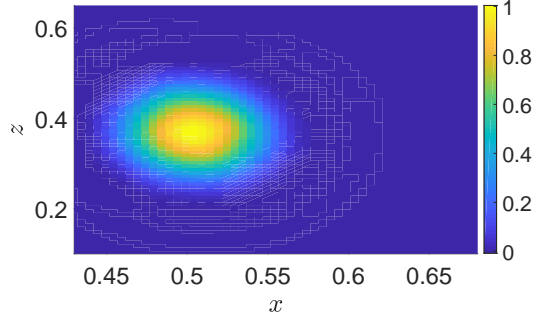
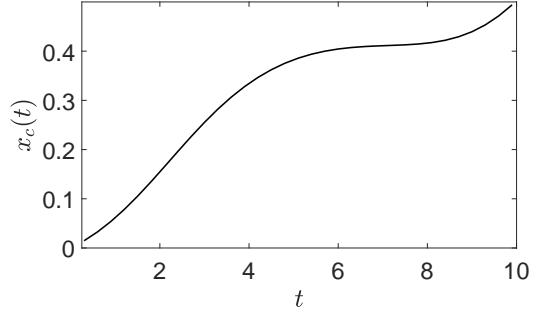


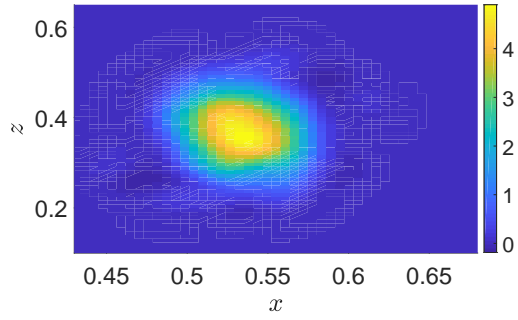
Figure 5: Comparisons of a cnoidal wave over a vortex patch(-) to a cnoidal wave over an irrotational fluid (- -) are shown on the left for various values of the Froude number F , while the relative energy change $\delta E(t)$ is shown on the right. Here $\mu = .2$, $\gamma = \sqrt{\mu}$, $t_f = 2/\mu$, $\tilde{m} = .6$, $\kappa = .43$.



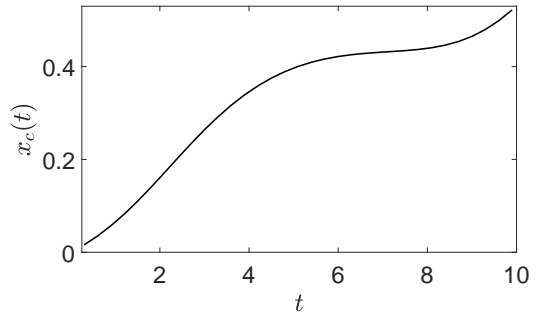
(a) $F = .01$



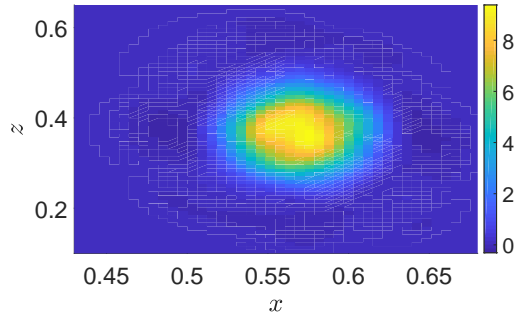
(b) $F = .01$



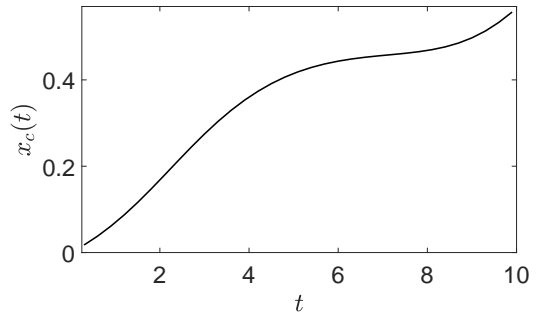
(c) $F = .05$



(d) $F = .05$



(e) $F = .1$



(f) $F = .1$

Figure 6: The vortex patches at the final time t_f for $F = .01$ (a), $F = .05$ (c), and $F = .1$ (e) and the motion of the horizontal center of mass $x_c(t)$ for $F = .01$ (b), $F = .05$ (d), and $F = .1$ (f) for $\tilde{m} = .6$ and $\kappa = .43$.

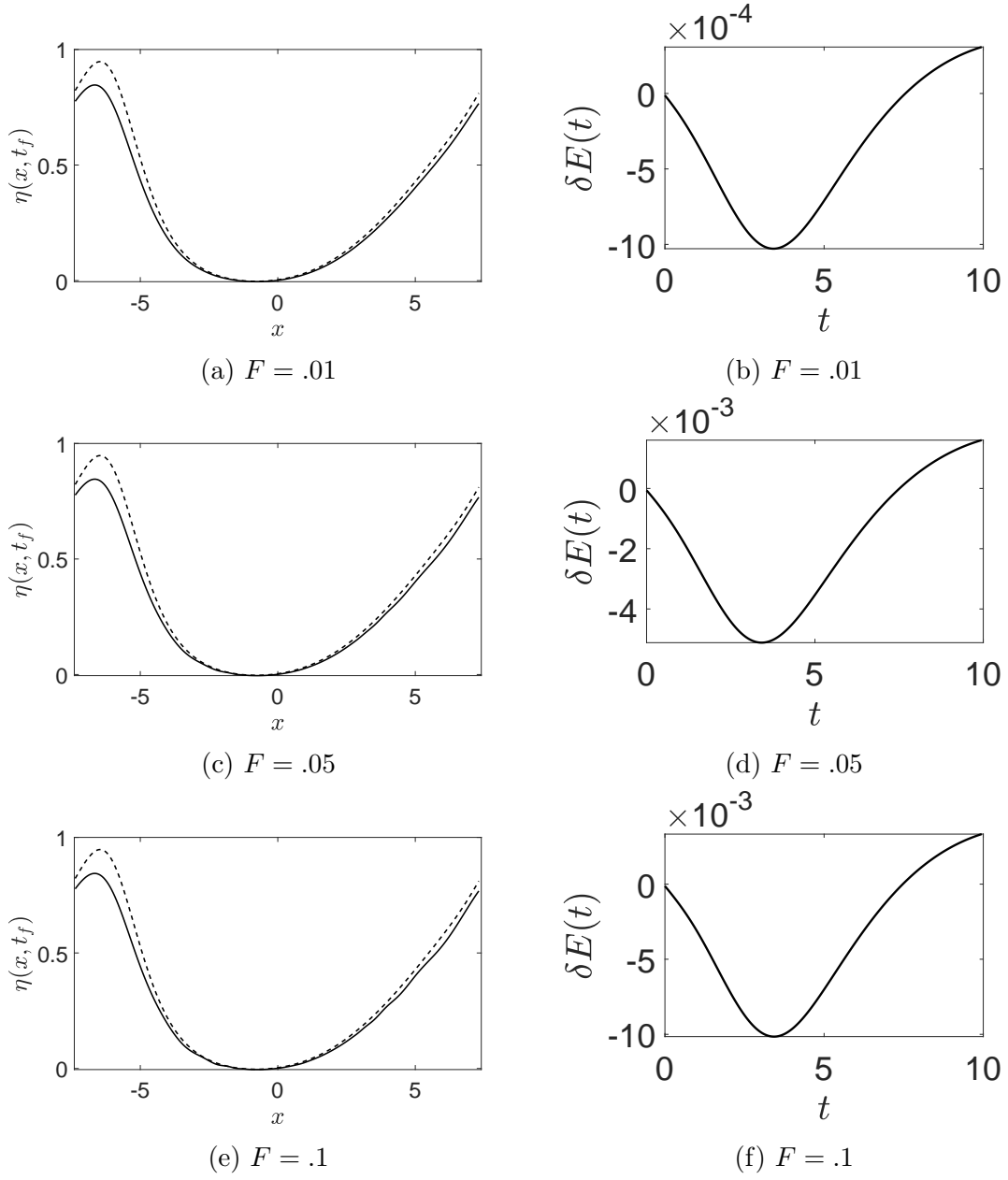


Figure 7: Comparisons of a cnoidal wave over a vortex patch(-) to a cnoidal wave over an irrotational fluid (- -) are shown on the left for various values of the Froude number F , while the relative energy change $\delta E(t)$ is shown on the right. Here $\mu = .2$, $\gamma = \sqrt{\mu}$, $t_f = 2/\mu$, $\tilde{m} = .9$, $\kappa = .35$.

cnoidal wave speed \tilde{c} varies from $\tilde{c} = -.1367$ for $\tilde{m} = .3$, $\kappa = .5$, to $\tilde{c} = .0506$ for $\tilde{m} = .9$, $\kappa = .35$. Thus, working in the fast coordinate and taking $\mu = .2$, we have a net wave speed of .9727 on the low side to 1.0101 on the high side. Therefore, there does not appear to be a significant enough variation in wave speed to explain the differences in the relative displacements of the vortex patches across all the cases studied in this paper. Thus, it appears that wave amplitude and width are the better determining factors for patch displacement, though the full nature of how these parameters interact with the Froude number is a subject of future study.

4 Conclusion

We have in this paper provided detailed numerical simulations of a vortex patch under a free-surface wave. This was done by bringing together approaches from both the nonlinear ocean waves and larger computational fluid dynamics community. Via our simulations, we have shown how vortex patches induce non-trivial deformations of propagating nonlinear waves coming from the shallow-water, KdV limit. The deformations are especially significant when the waves are low amplitude, essentially linear modes. Our simulations allow for greater quantitative insight by tracking the relative energy transfer of the patch to the wave, the dynamics and features of which we show correlates strongly to the presence or absence of significant deformations in the surface wave due to the vortex patch.

Acknowledgements

Appendix

Details about the Derivation of Bernoulli's Equation

To derive Equation (2), we make use of a result in [40], which shows, making no assumption on the behavior of the vorticity, that the following conservation law holds at the free surface $y = \eta(x, t)$

$$\partial_t \mathcal{C} + \partial_x \left(u\mathcal{C} + g\eta - \frac{1}{2} |\mathbf{u}|^2 \right) = 0, \quad \mathcal{C} = \mathbf{u} \cdot (1, \partial_x \eta), \quad \mathbf{u} = (u, w).$$

Assuming the compactly supported vortex patch $\omega(x, y, t)$ does not intersect the free surface, we can then write the fluid velocity $\mathbf{u} = \nabla \bar{\phi}$, where

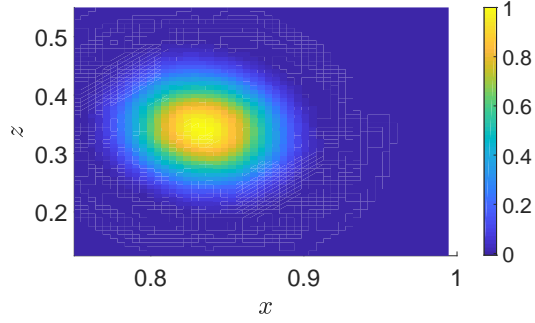
$$\bar{\phi} = \phi_v + \tilde{\phi}, \quad \phi_v(\mathbf{x}, t) = \int_{\Omega} \tilde{K}(\mathbf{x}, \tilde{\mathbf{x}}) \omega(\tilde{\mathbf{x}}, t) d\tilde{\mathbf{x}}$$

where \tilde{K} is the associated harmonic conjugate to the stream function which defines the Biot-Savart kernels and the periodic extensions thereof. We readily see then that

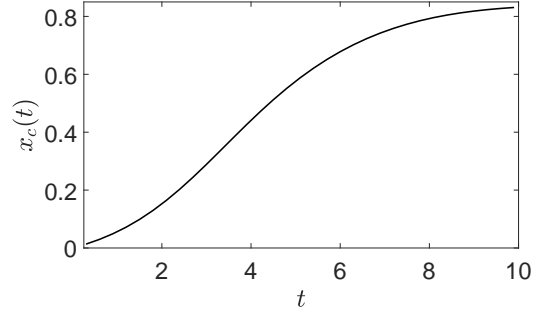
$$\mathcal{C} = \partial_x \bar{\phi} \big|_{y=\eta}.$$

Integrating the conservation law in x and setting the associated integration constant to zero then gives us the Bernoulli equation for $\bar{\phi}$ at $y = \eta$ i.e.

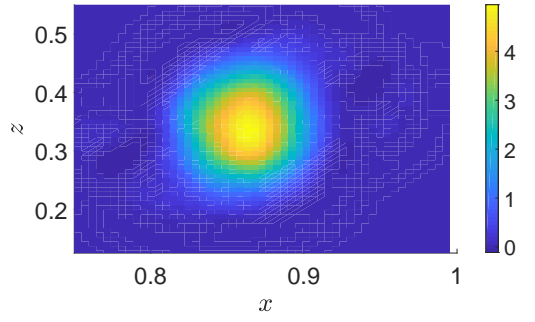
$$\partial_t \bar{\phi} + \frac{1}{2} |\nabla \bar{\phi}|^2 + g\eta = 0, \quad y = \eta(x, t).$$



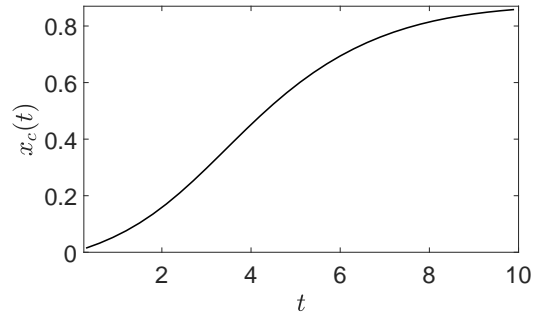
(a) $F = .01$



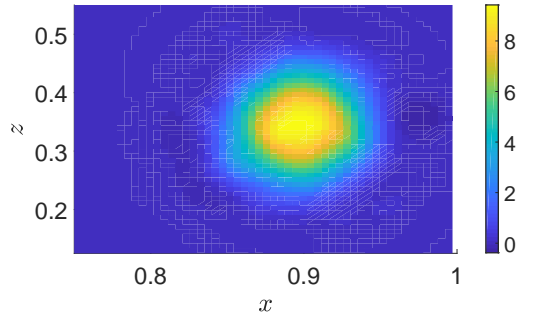
(b) $F = .01$



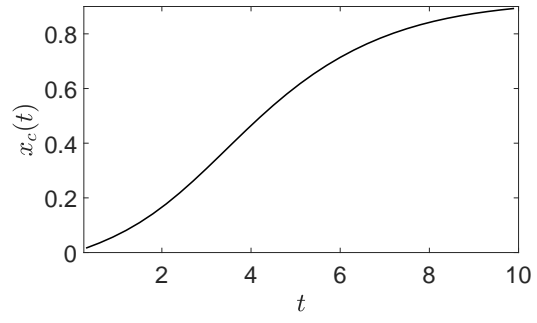
(c) $F = .05$



(d) $F = .05$



(e) $F = .1$



(f) $F = .1$

Figure 8: The vortex patches at the final time t_f for $F = .01$ (a), $F = .05$ (c), and $F = .1$ (e) and the motion of the horizontal center of mass $x_c(t)$ for $F = .01$ (b), $F = .05$ (d), and $F = .1$ (f) for $\tilde{m} = .9$ and $\kappa = .35$.

Using the PVM to discretize ω and ignoring the mollification then gives Equation (2), though see [30] for more details.

Details about the DNO

We here provide details about the Dirichlet-to-Neumann Operator (DNO) for the sake of completeness; see [32, 33] for greater details. The DNO $G(\eta)$ in the shallow-water scalings used throughout the body of the paper is found via expanding in powers of η so that the kinematic condition becomes

$$\eta_t - \frac{1}{\gamma} P_v(x, 1 + \mu\eta, t) = (G_0 + \mu G_1 + \mu^2 G_2 + \cdots) Q.$$

Defining the Fourier transform of a periodic function $f(x)$ to be \hat{f} , so that

$$\hat{f}(k) = \frac{1}{2M} \int_{-M}^M f(x) e^{-i\pi k x} dx, \quad k \in \mathbb{Z},$$

we define, for a linear operator L , its associated symbol $\hat{L}(k)$ by way of the formula

$$\hat{L}(k) \hat{f}(k) = \frac{1}{2M} \int_{-M}^M L f(x) e^{-i\pi k x / M} dx.$$

We then get

$$\hat{G}_0(k) = -\frac{i}{\gamma} \tanh(\pi \gamma k),$$

and, for $m \geq 1$,

$$\begin{aligned} G_m Q = & - \sum_{j=1}^{\lfloor m/2 \rfloor} \frac{1}{(2j)!} D_\gamma^{2j} (\eta^{2j} G_{m-2j} Q) \\ & - \gamma^2 \partial_x G_0 \sum_{j=0}^{\lfloor (m-1)/2 \rfloor} \frac{D_\gamma^{2j}}{(2j+1)!} (\eta^{2j+1} G_{m-2j-1} Q) - \frac{1}{m!} L_m \partial_x D_\gamma^{m-1} (\eta^m Q), \end{aligned}$$

where

$$\hat{D}_\gamma = \pi \gamma k,$$

and

$$\hat{L}_m = \begin{cases} 1, & m \text{ is odd,} \\ i\gamma \hat{G}_0(k), & m \text{ is even.} \end{cases}$$

This recursive formula is readily computable, and for the shallow-water scalings we pick, achieving machine-precision is relatively straightforward.

References

- [1] A. Constantin. *Nonlinear Water Waves with Applications to Wave-Current Interactions and Tsunamis*. SIAM, Philadelphia, 2011.
- [2] H. Lamb. *Hydrodynamics*. Dover, New York, N.Y., 1945.
- [3] P.K. Kundu, I.M. Cohen, and D.R. Dowling. *Fluid Mechanics*. Elsevier, New York, N.Y., 5 edition, 2012.
- [4] L.H. Holthuijsen. *Waves in Oceanic and Coastal Waters*. Cambridge University Press, Cambridge, 2007.
- [5] D.I. Pullin and R. Grimshaw. Nonlinear interfacial progressive waves near a boundary in a Boussinesq fluid. *Phys. Fluid.*, 26:897, 1983.
- [6] J.A. Simmen and P.G. Saffman. Steady deep-water waves on a linear shear current. *Stud. Appl. Math.*, 75:35–57, 1985.
- [7] A.F. Teles da Silva and D.H. Peregrine. Steep, steady surface waves on water of finite depth with constant vorticity. *J. Fluid Mech.*, 195:281–302, 1988.
- [8] A.D.D. Craik. The generalized Lagrangian-mean equations and hydrodynamic stability. *J. Fluid Mech.*, 125:27–35, 1982.
- [9] A.D.D. Craik. Wave-induced longitudinal-vortex instability in shear flows. *J. Fluid Mech.*, 125:37–52, 1982.
- [10] P. Drazin and W. Reid. *Hydrodynamic Stability*. Cambridge University Press, Cambridge, 1981.
- [11] W.R.C. Phillips. On the spacing of Langmuir circulation in strong shear. *J. Fluid Mech.*, 525:215–236, 2005.
- [12] O. Nwogu. Interaction of finite-amplitude waves with vertically sheared current fields. *J. Fluid Mech.*, 627:179–213, 2009.
- [13] K.A. Chang, T.J. Hsu, and P.L.F. Liu. Vortex generation and evolution in water waves propagating over a submerged rectangular obstacle. Part I: Solitary waves. *Coast. Eng.*, 44:13–36, 2001.
- [14] K.A. Chang, T.J. Hsu, and P.L.F. Liu. Vortex generation and evolution in water waves propagating over a submerged rectangular obstacle. Part II: Cnoidal waves. *Coast. Eng.*, 52:257–283, 2005.
- [15] C. Lin, T.C. Ho, S.C. Chang, S.C. Hsieh, and K.A. Chang. Vortex shedding induced by a solitary wave propagating over a submerged vertical plate. *Int. J. Heat and Fluid Flow*, 26:894–904, 2005.

- [16] O. Nwogu. Alternative form of Boussinesq equations for nearshore wave propagation. *J. Waterw. Port Coastal Eng.*, 119:618–638, 1993.
- [17] Q. Chen, J.T. Kirby, R.A. Dalrymple, and F. Shi and. Boussinesq modeling of longshore currents. *J. Geophys. Res.*, 108:26–43, 2003.
- [18] Y. Zhang, A.B. Kennedy, N. Panda, C. Dawson, and J.J. Westerink. Boussinesq-Green-Naghdi rotational water wave theory. *Coastal Eng.*, 73:13–27, 2013.
- [19] A. Castro and D. Lannes. Well-posedness and shallow-water stability for a new Hamiltonian formulation of the water waves equations with vorticity. *Indiana Univ. Math. J.*, 64:1169–1270, 2014.
- [20] A. Castro and D. Lannes. Fully nonlinear long-wave models in the presence of vorticity. *J. Fluid Mech.*, 759:642–675, 2014.
- [21] D. Lannes and F. Marche. Nonlinear wave-current interactions in shallow water. *Stud. Appl. Math.*, 136:382–423, 2016.
- [22] G.H. Cottet and P.D. Koumoutsakos. *Vortex Methods: Theory and Practice*. Cambridge University Press, Cambridge, 2000.
- [23] P. Koumoutsakos and A. Leonard. High-resolution simulations of the flow around an impulsively started cylinder using vortex methods. *J. Fluid Mech.*, 296:1–38, 1995.
- [24] P. Koumoutsakos. Inviscid axisymmetrization of an elliptical vortex. *J. Comp. Phys.*, 138:821–857, 1997.
- [25] R. Krasny. Vortex sheet computations: Roll-up, waves, separation. *Lec. Appl. Math.*, 28:385–402, 1991.
- [26] J.T. Beale and A. Majda. High order accurate vortex methods with explicit velocity kernels. *J. Comp. Phys.*, 58:188–208, 1985.
- [27] A.J. Majda and A.L. Bertozzi. *Vorticity and Incompressible Flow*. Cambridge University Press, Cambridge, 2002.
- [28] P. Koumoutsakos. Multiscale flow simulations using particles. *Ann. Rev. Fluid Mech.*, 37:457–487, 2005.
- [29] W.M. van Rees, A. Leonard, D.I. Pullin, and P. Koumoutsakos. A comparison of vortex and pseudo-spectral methods for the simulation of periodic vorical flows at high Reynolds numbers. *J. Comp. Phys.*, 230:2794–2805, 2011.
- [30] C.W. Curtis and H. Kalisch. Vortex dynamics in free-surface flows. *Phys. Fluids*, 29:032101, 2017.
- [31] M.J. Ablowitz, A.S. Fokas, and Z.H. Musslimani. On a new non-local formulation of water waves. *J. Fluid Mech.*, 562:313–343, 2006.

- [32] W. Craig and C. Sulem. Numerical simulation of gravity waves. *J. Comput. Phys.*, 108:73–83, 1993.
- [33] P. Guyenne and D.P. Nicholls. A high-order spectral method for nonlinear water waves over moving bottom topography. *SIAM J. Sci. Comput.*, 30:81–101, 2007.
- [34] L. Greengard and V. Rokhlin. A fast algorithm for particle simulations. *J. Comp. Phys.*, 73:325–348, 1987.
- [35] P.G. Saffman. *Vortex Dynamics*. Cambridge University Press, Cambridge, 1992.
- [36] G.H. Cottet. A new approach for the analysis of vortex methods in 2 and 3 dimensions. *Ann. Inst. Henri Poincaré*, 5:227–285, 1988.
- [37] J. Wilkening and V. Vasan. Comparison of five methods of computing the Dirichlet–Neumann operator for the water wave problem. In *Nonlinear Wave Equations: Analytic and Computational Techniques*. AMS, 2015.
- [38] D.P. Nicholls and F. Reitich. Stability of high-order perturbative methods for the computation of Dirichlet–Neumann operators. *J. Comp. Phys.*, 170:276–298, 2001.
- [39] V.E. Zakharov. Stability of periodic waves of finite amplitude on the surface of a deep fluid. *Zhurnal Prikladnoi Mekhaniki i Tekhnicheskoi Fiziki*, 8:86–94, 1968.
- [40] S. Gavriluk, H. Kalisch, and Z. Khorsand. A kinematic conservation law in free surface flow. *Nonlinearity*, 28:1805–1821, 2015.